Electronic Supplementary Material (ESI) for Lab on a Chip.

A microfluidic approach for probing hydrodynamic effects in scale formation

Ricardo D. Sosa,[a] Xi Geng,[a] Michael A. Reynolds,[b] Jeffrey D. Rimer,[a,*] Jacinta C. Conrad[a,*]

* Corresponding authors: jrimer@central.uh.edu, jcconrad@uh.edu

[a] Department of Chemical and Biomolecular Engineering, University of Houston, Houston, TX 77204-4004, USA

[b] Shell Exploration and Production Company, Royal Dutch Shell, plc, Houston, TX 77082, USA

Supplementary results and figures

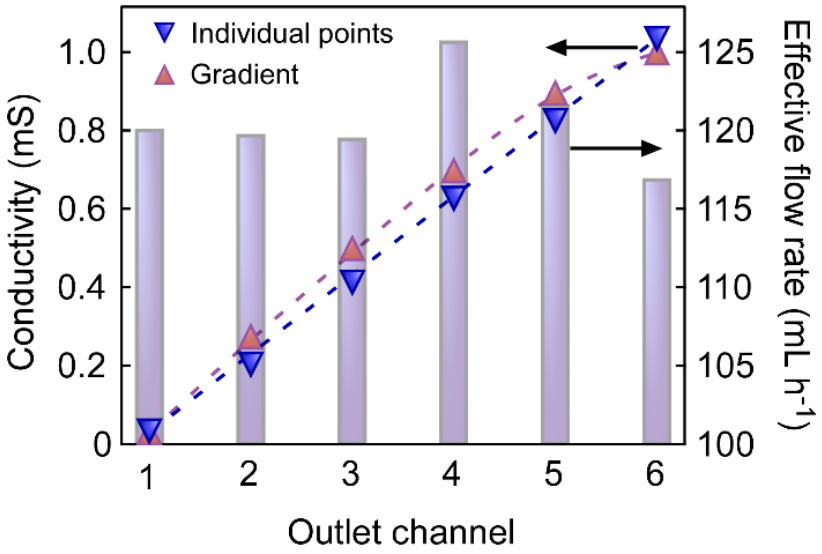

Figure S1: (Left axis, points) Ion concentration profile of Ba^{2+} (conductivity) of microchannel effluent. Conductivity measurements of the ion flux of $BaCl_2$ (aq) in each channel effluent are represented by the pink and blue data points. Conductivity measurements were obtained for both effluents from the gradient generator and for individual microchannels. Dashed lines are guides-to-the-eye. (Right axis, purple bars) Effective flow rate in each outlet channel, determined by timing the collection of effluent. All data correspond to a single experiment.

Characterization of the gradient generator. The accuracy of the microfluidic gradient generator was examined by collecting and characterizing the six outlet effluents after flowing aqueous $BaCl_2$ in one inlet and DI water in the second inlet. Inlets were flowed into the

microfluidic device using a dual syringe pump at a total flow rate of 720 mL h^{-1} to produce a flow rate of 120 mL h^{-1} in each outlet stream. The mass of effluents was measured after 10 min of collection using a Mettler Toledo balance. The effective flow rate, determined for each outlet was close to the theoretical value (120 mL h^{-1}) (Figure S1). The accuracy of the concentration gradient generator was determined by comparing the measured ion flux (mS) in each effluent against individually prepared $BaCl_2$ aqueous solutions within the concentration range tested. Conductivity measurements were obtained using a VWR International conductivity meter. The conductivity of effluents from each channel are the same, within experimental error, as the conductivity of solutions prepared at several concentrations within the expected range, suggesting the gradient generator can successfully mix and split streams to obtain effluents corresponding to a linear concentration gradient.

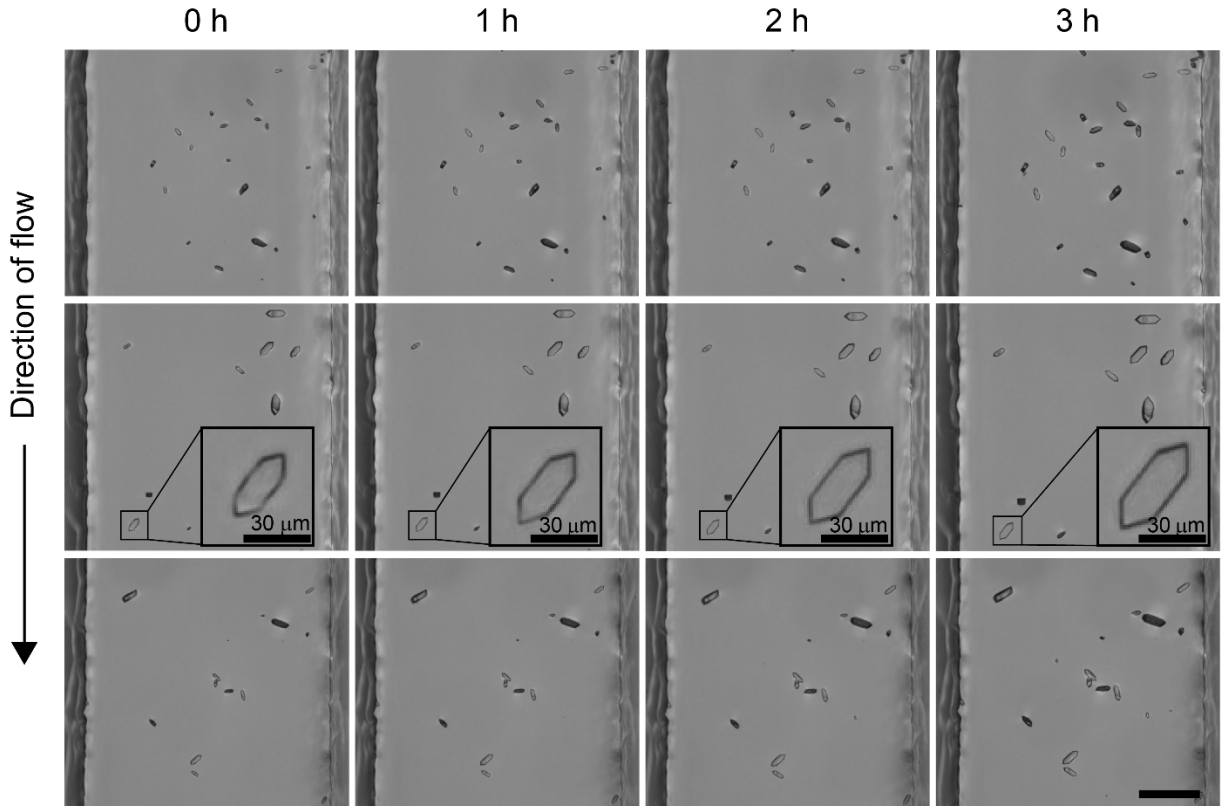

Figure S2: Large area field of view micrographs showing time-elapsed growth of barite seed crystals in the microchannel under flow of a supersaturated growth solution (12 mL h^{-1}, $S = 7$). The scale bar indicates 100 μm for all images unless otherwise stated. Insets depict enlarged micrographs that show the growth of a single crystal.

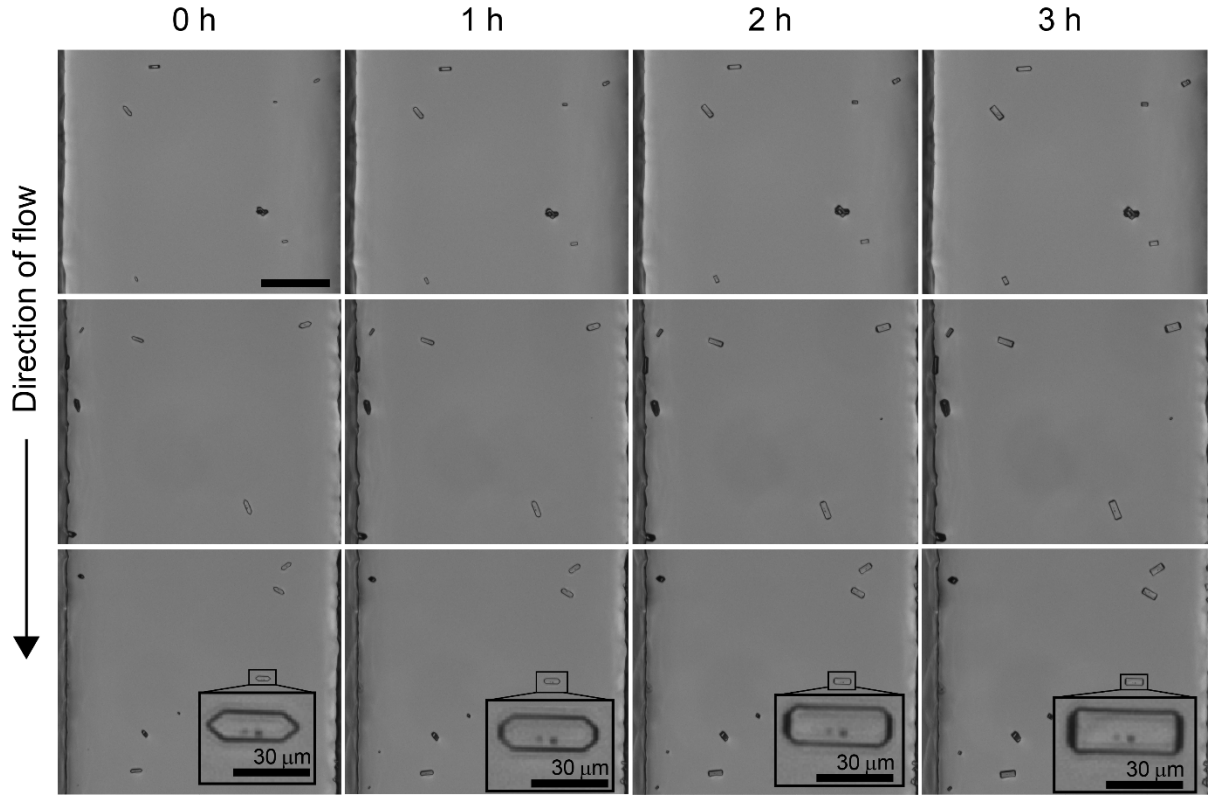

Figure S3: Large area field of view micrographs showing time-elapsed growth of barite seed crystals in the microchannel under flow of a supersaturated growth solution (12 mL h^{-1}, $S = 7$) in the presence of 1 μg mL^{-1} DTPA. The scale bar indicates 100 μm for all images unless otherwise stated. Insets depict enlarged micrographs that show the inhibitory effect of DTPA on a single crystal.

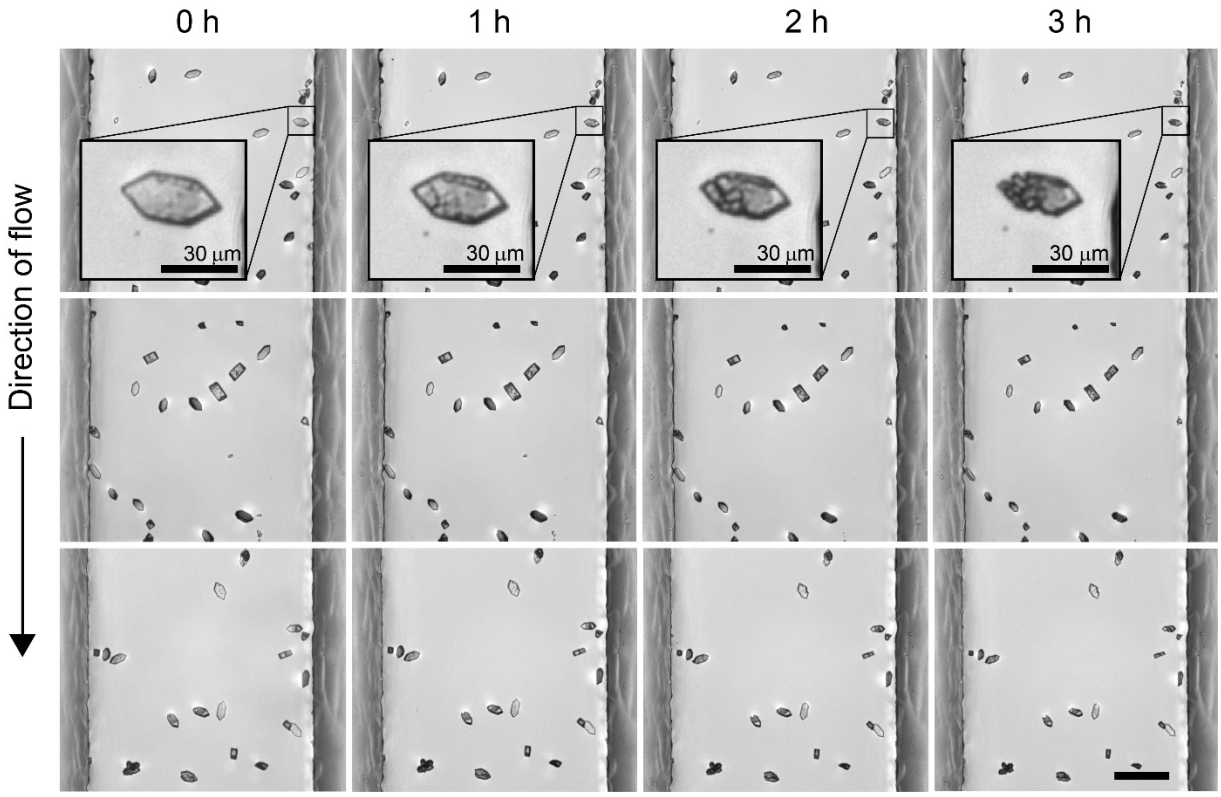

Figure S4: Large area field of view micrographs showing time-elapsed dissolution of barite seed crystals in the microchannel under flow of alkaline solution (12 mL h^{-1}, pH = 9) in the presence of 200 μg mL^{-1} DTPA. The scale bar indicates 100 μm for all images unless otherwise stated. Insets depict enlarged micrographs that show the effect of DTPA on the dissolution of a single crystal.

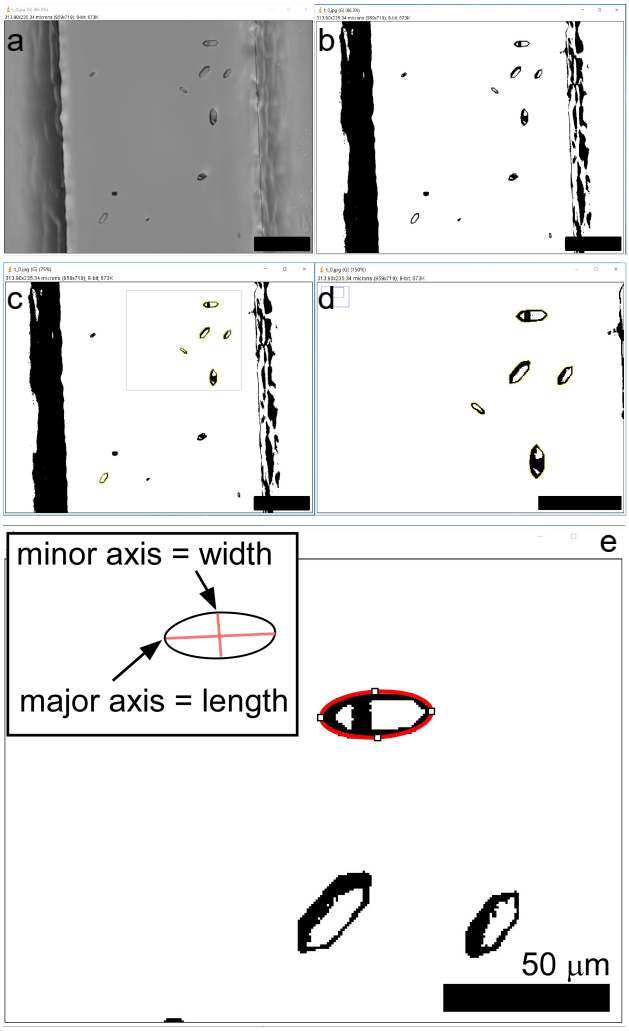

Figure S5: (a) Grey scale micrograph used for analysis in the ImageJ user interface. (b) Conversion of grey scale micrograph to black and white. (c) Selection of crystals for size measurements using wand tool. (d) Enlarged micrograph showing the outline of wand tool selection (yellow perimeter). (e) Enlarged micrograph showing the ellipse fit to the crystal selection and the ellipse parameters used for length and width measurements. Scale bars in (a) – (d) are equal to 100 μm.

The micrograph in Figure S5a depicts a region of the microchannel loaded with barite seed crystals. The gray scale image is converted to black and white (Figure S5b) to allow for edge detection in ImageJ. The wand tool is then used to outline the outer perimeter of the crystals and single crystal measurements are taken. The images above show the edge detection capabilities of ImageJ for the micrographs used to obtain crystal size measurements. A given crystal is selected by clicking on the outside of the crystal to the left. The wand tool traces the object of uniform color

(black crystal perimeter) and can automatically measure the crystal length and width by fitting an ellipse. The image in Figure S5c depicts the width of the microchannel and the crystals selected for measurement. Figure S5d depicts a higher magnification image of the region in Figure S5c to show the outlining of the crystals using the wand tool, which appears as a yellow perimeter. The high-magnification image in Figure S5e focuses on the three crystals from Figure S5d. One representative crystal is highlighted for measurement. An ellipse is fit to the crystal for measurement of the crystal aspect ratio. The inset in Figure S5e shows the ellipse fit to the crystal. The ellipse major axis and minor axis are taken as the length and width of crystals, respectively.

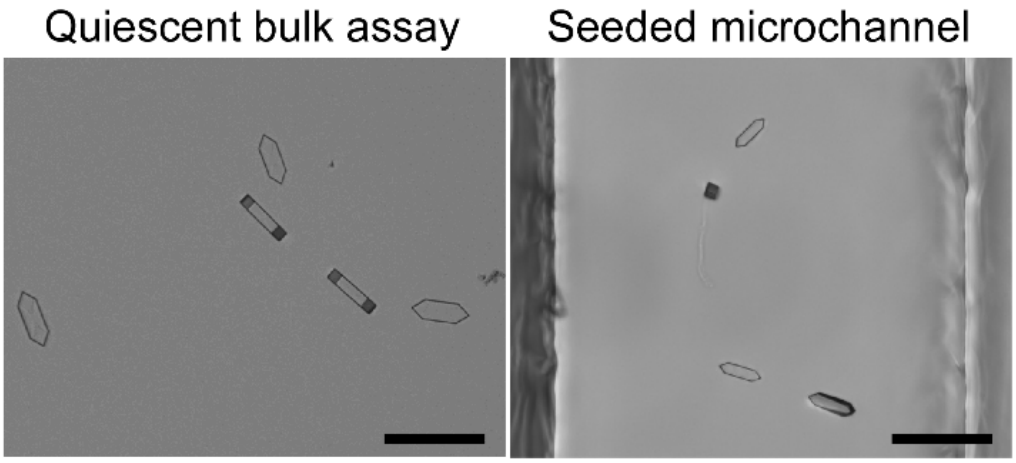

Figure S6: Optical micrographs of barite crystals grown (left) in vials and (right) in microchannels exhibit identical morphologies. Scale bars are equal to 100 μm.

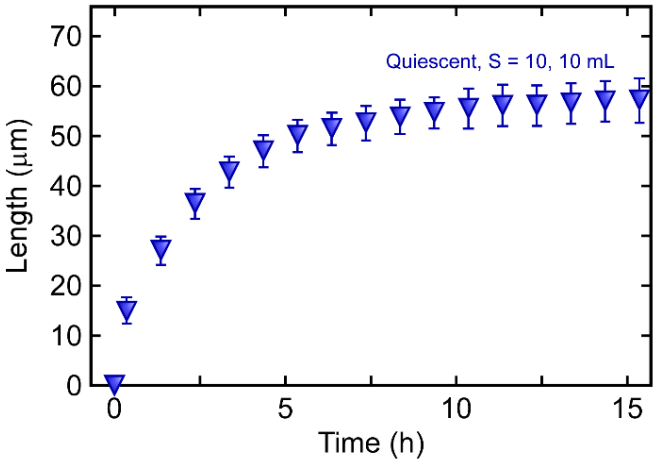

Figure S7: Growth kinetics for bulk crystallization assays under quiescent conditions and supersaturation ratio $S = 10$. Temporal changes in crystal length along the [010] direction were monitored for 15 h at room temperature to quantify the kinetics of crystal growth. Length measurements (symbols) represent an average of at least three individual experiments (for at least 30 crystals per experiment) and error bars indicate two standard deviations across experiments.

Growth kinetics for bulk crystallization. The length of barite crystals synthesized in 20 mL glass vials was captured from the earliest observable point of nucleation, by optical microscopy, for a 15-h period during which equilibrium appears to be established between the crystals and bulk medium. The growth rate was greater within the first 5 h, after which the length begins to approach a plateau at ~60 μm due to the depletion of solute.

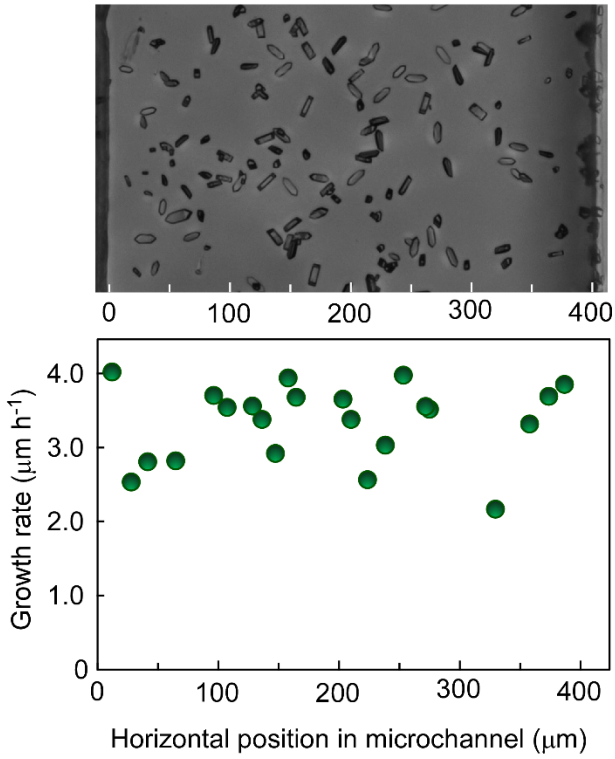

Figure S8: Growth kinetics as a function of position across the microchannel. (top) Representative optical micrograph of barite seed crystals in the microchannel. (bottom) Single crystal growth kinetics of barite seed crystals in the micrograph. Seed crystals were tracked by their horizontal position relative to the left wall of the microchannel.

Homogeneous growth within microfluidic channels. The synthesis of seed crystals and growth rates in subsequent experiments were homogeneous across the width of the microchannels (Figure S8), consistent with the advection dominance at the flow rates used in all experiments. The optical micrograph in Figure S8 depicts a representative region of a seeded microchannel. Crystal growth rates across the width of the microchannel demonstrate no observable trend as a function of horizontal position in the microchannel, indicating there is complete mixing of growth solution within the channel and no diffusion limitations.

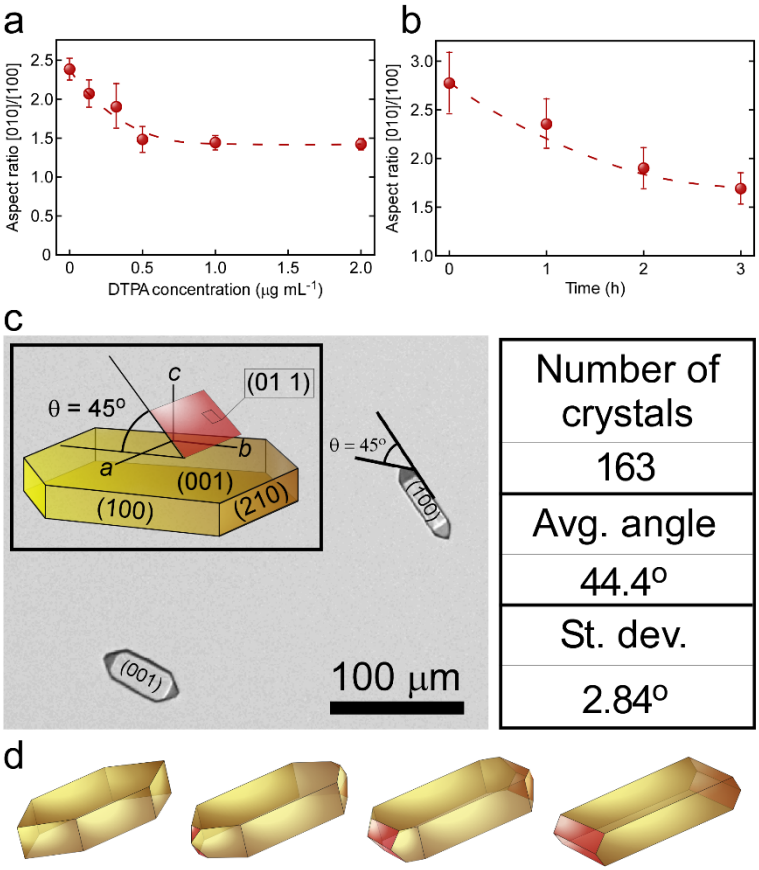

Figure S9: Analysis of the development of (011) facets in the presence of DTPA. (a) Aspect ratio of the basal surface measured as a function of increasing concentration of DTPA at the end of 3-h experiments under flow (12 mL h^{-1}) of supersaturated solutions (S = 7) in the microchannels. (b) Aspect ratio of the (001) basal surface over time under flow (12 mL h^{-1}) of growth solution (S = 7) with fixed 0.5 μg mL^{-1} DTPA. Data points in (a) and (b) represent average measurements for at least 100 crystals; and error bars indicate two standard deviations. (c) Optical micrograph analysis of {011} facets through measurements of dihedral angles. (d) Schematic illustrating the transformation of barite morphology over time in the presence of DTPA in supersaturated growth media.

Transformation of barite morphology. Barite inhibition in the presence of DTPA resulted in crystals with a morphology differing from the control. The measured aspect ratio decreased as a function of either DTPA concentration or time (Figure S9a and b), suggesting binding specificity near the apex of the crystals. Optical micrographs in which the (100) face of barite crystals was exposed suggest the apex is not completely blunted. Furthermore, a new facet develops, which intersects the (010) and (001) planes. The angle of the newly developed facet with respect to the

(001) plane was measured to be ~45° (Figure S9c), suggesting the new facet corresponds to the (011) surface. The transformation of the morphology is illustrated schematically in Figure S9d.

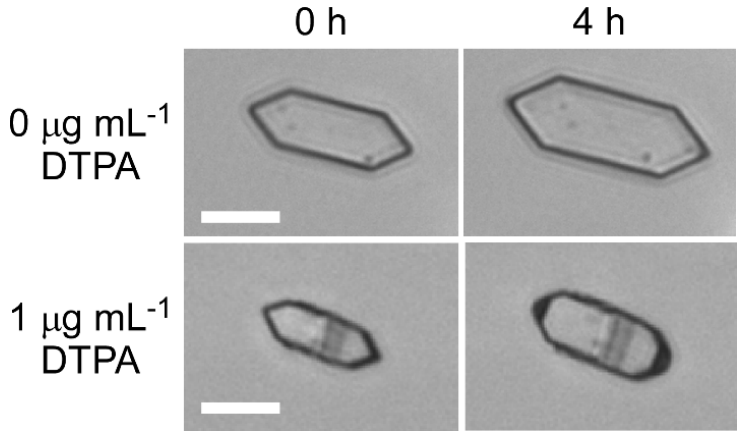

Figure S10: Optical micrographs of barite crystals at 0 h (left column) and 4 h (right column) under 1.2 mL h^{-1} flow of growth solutions (S=7) in the absence (top row) and presence (bottom row) of DTPA. Scale bars indicate 10 μm.

Boundary layer analysis. The Schmidt number (Sc) represents the ratio of the rates of viscous diffusion to molecular diffusion. For $Sc \gg 1$, the diffusion boundary layer is much thinner than the hydrodynamic boundary layer. For $DTPA_{(aq)}$, $D \approx 1 \times 10^{-9}$ m^2 s^{-1} and $\nu \approx 9.06 \times 10^{-7}$ m^2 s^{-1}, and the dimensionless quantity $Sc \approx 850$. Thus, the diffusion boundary layer thickness can be approximated by $\delta \approx 5\left(\frac{D}{\nu}\right)^{\frac{1}{3}}\left(\frac{Wx}{Re}\right)^{\frac{1}{2}}$ (eq. 2 in the main text), where x is the average length of the crystals and U_0 is the maximum fluid velocity.

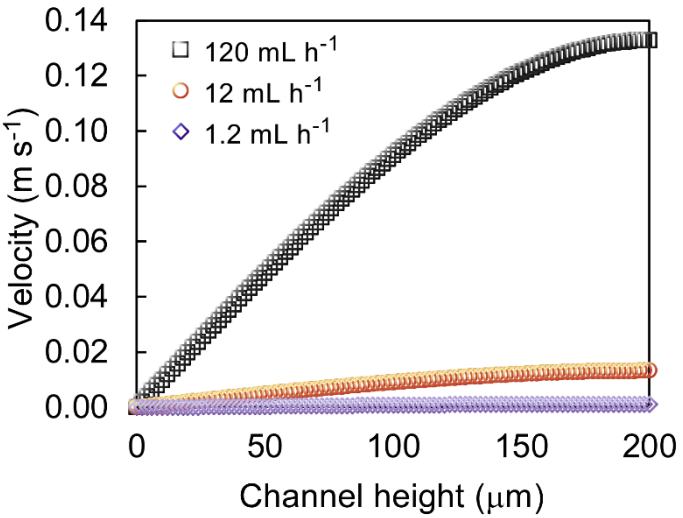

Figure S11: Velocity profiles through the microchannels for various flow rates (symbols) along channel height. From the von Kármán momentum balance, velocity profiles can be approximated as $\frac{v_x}{v_\infty} = \frac{3}{2}\left(\frac{y}{\delta}\right) - \frac{1}{2}\left(\frac{y}{\delta}\right)^3$, where y is the dimension along the channel height and $\delta = 4.64\sqrt{\frac{\nu x}{U_0}}$. U_0 is the maximum fluid velocity in the microchannel and x is the position along the length of the microchannel.

a

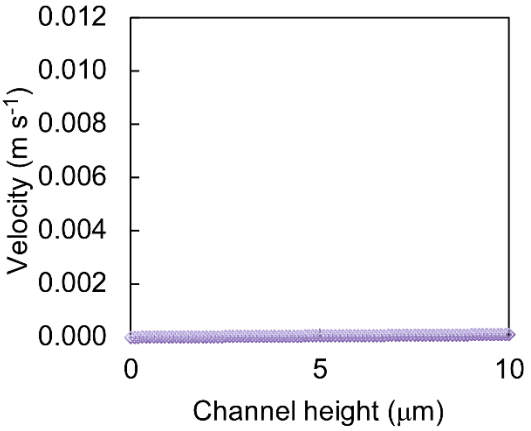

b

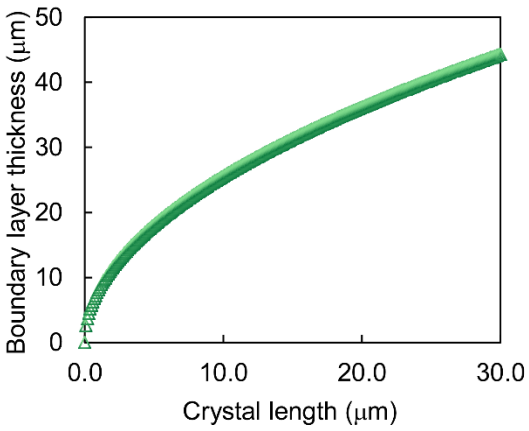

c

Crystal length (μm)	Concentration boundary layer thickness (μm)	Boundary layer velocity (μm s^{-1})
0	0.0	0.00
5	18	180
10	26	250
15	31	310
20	36	360
25	41	400
30	44	430

Figure S12: (a) Velocity profile for aqueous DTPA flowing through the microchannel at 1.2 mL h^{-1}. (b) Concentration diffusion boundary layer thickness as a function of crystal length for 1.2 mL h^{-1}. (c) Fluid velocity at the outer edge of the boundary layer for different locations along the crystal length.

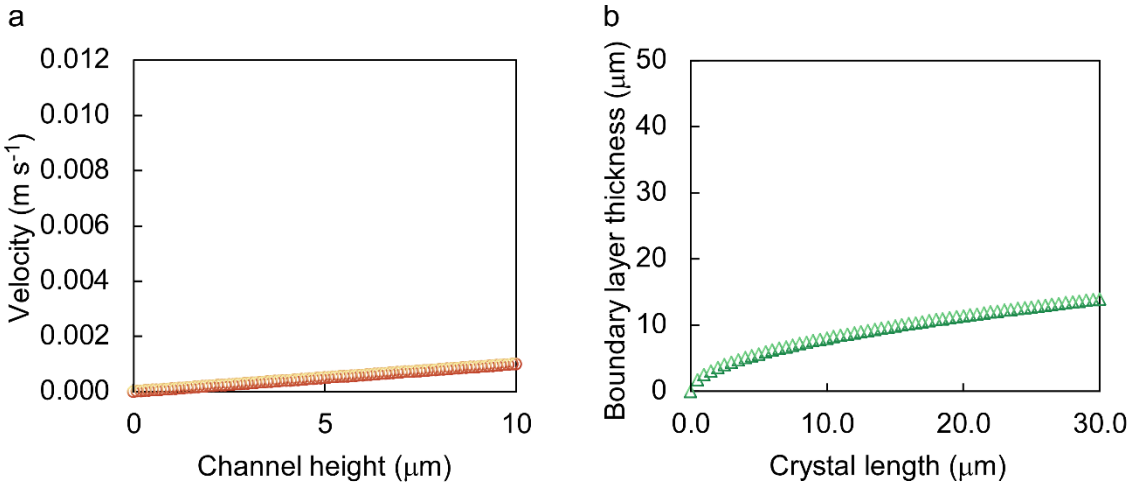

c

Crystal length (μm)	Concentration boundary layer thickness (μm)	Boundary layer velocity (μm s^{-1})
0	0.0	0.00
5	5.7	570
10	8.1	810
15	9.9	990
20	12	1100
25	13	1300
30	14	1400

Figure S13: (a) Velocity profile for aqueous DTPA flowing through the microchannel at 12 mL h^{-1}. (b) Concentration diffusion boundary layer thickness as a function of crystal length for 12 mL h^{-1}. (c) Fluid velocity at the outer edge of the boundary layer for different locations along the crystal length.

a

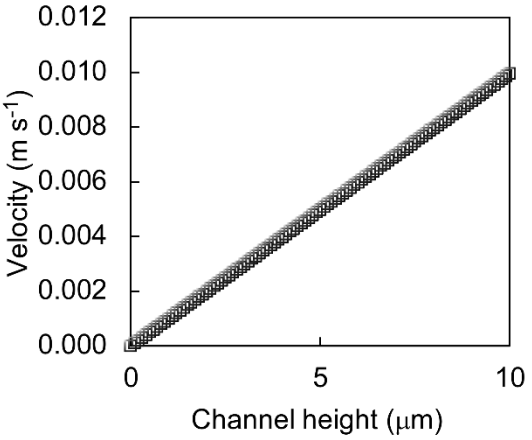

b

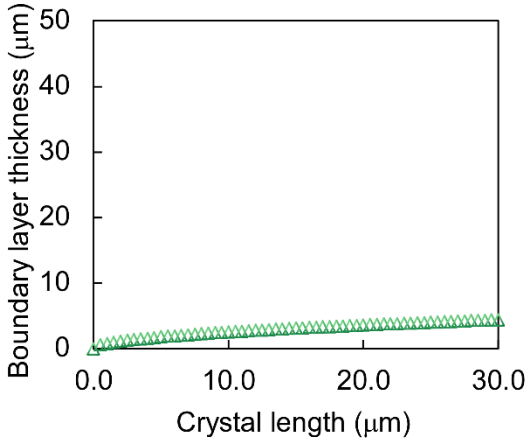

c

Crystal length (μm)	Concentration boundary layer thickness (μm)	Boundary layer velocity (μm s^{-1})
0	0.0	0.00
5	1.8	1800
10	2.6	2600
15	3.1	3100
20	3.6	3600
25	4.1	4000
30	4.4	4400

Figure S14: (a) Velocity profile for aqueous DTPA flowing through the microchannel at 120 mL h^{-1}. (b) Concentration diffusion boundary layer thickness as a function of crystal length for 120 mL h^{-1}. (c) Fluid velocity at the outer edge of the boundary layer for different locations along the crystal length.

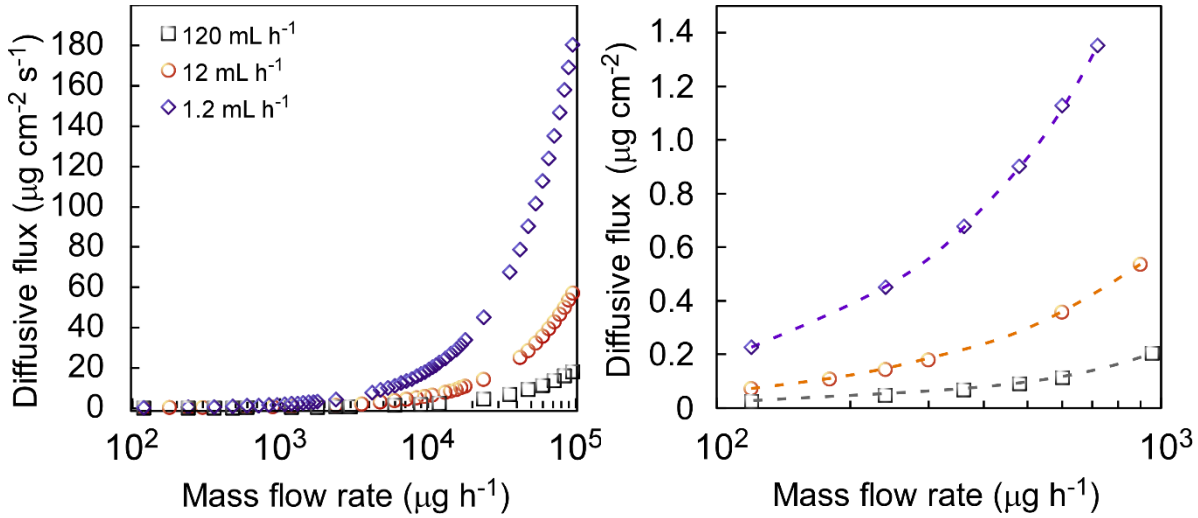

Figure S15: Diffusive flux of DTPA as a function of the DTPA mass flow rate. The molecular diffusional flux is of the order of magnitude $J = \frac{Dc_0}{\delta}$. The diffusional flux was calculated for each combination of flow rate and concentration, using the boundary layer based on the flow rate. (left) Full mass flow rate range; (right) small range of mass flow rates, to distinguish the diffusive flux curves for each flow rate.